Frequency-diverse microwave imaging using planar Mills-Cross cavity apertures

Okan Yurduseven,* Jonah N. Gollub, Daniel L. Marks, and David R. Smith

Center for Mematerials and Integrated Plasmonics, Department of Electrical and Computer Engineering, Duke University, Durham, 27708, North Carolina, USA
okan.yurduseven@duke.edu

Abstract: We demonstrate a frequency diverse, multistatic microwave imaging system based on a set of transmit and receive, radiating, planar cavity apertures. The cavities consist of double-sided, copper-clad circuit boards, with a series of circular radiating irises patterned into the upper conducting plate. The iris arrangement is such that for any given transmitting and receiving aperture pair, a Mills-Cross pattern is formed from the overlapped patterns. The Mills-Cross distribution provides optimum coverage of the imaging scene in the spatial Fourier domain (k-space). The Mills-Cross configuration of the apertures produces measurement modes that are diverse and consistent with the computational imaging approach used for frequency-diverse apertures, yet significantly minimizes the redundancy of information received from the scene. We present a detailed analysis of the Mills-Cross aperture design, with numerical simulations that predict the performance of the apertures as part of an imaging system. Images reconstructed using fabricated apertures are presented, confirming the anticipated performance.

OCIS codes: (110.0110) Imaging systems; (110.1220) Apertures; (350.4010) Microwaves; (110.1650) Coherence imaging; (110.1758) Computational imaging; (110.2970) Image detection systems.

References and links

1. A. W. Doerry and F. M. Dickey, "Synthetic aperture radar," Opt. Photonics News **15**(11), 28–33 (2004).
2. A. Moreira, P. Prats-Iraola, M. Younis, G. Krieger, I. Hajnsek, and K. P. Papathanassiou, "A tutorial on synthetic aperture radar," IEEE Geosci. Rem. Sens. Mag. **1**(1), 6–43 (2013).
3. N. K. Nikolova, "Microwave imaging for breast cancer," IEEE Microw. Mag. **12**(7), 78–94 (2011).
4. M. Fallahpour, J. T. Case, M. T. Ghasr, and R. Zoughi, "Piecewise and Wiener filter-based SAR techniques for monostatic microwave imaging of layered structures," IEEE Trans. Antenn. Propag. **62**(1), 282–294 (2014).
5. Y. Wang and A. E. Fathy, "Advanced system level simulation platform for three-dimensional UWB through-wall imaging SAR using time-domain approach," IEEE Trans. Geosci. Rem. Sens. **50**(5), 1986–2000 (2012).
6. S. Demirci, H. Cetinkaya, E. Yigit, C. Ozdemir, and A. A. Vertiy, "A study on millimeter-wave imaging of concealed objects: application using back-projection algorithm," Prog. Electromagnetics Res. **128**, 457–477 (2012).
7. F. Qi, I. Ocket, D. Schreurs, and B. Nauwelaers, "A system-level simulator for indoor mmW SAR imaging and its applications," Opt. Express **20**(21), 23811–23820 (2012).
8. J. A. Martinez-Lorenzo, F. Quivira, and C. M. Rappaport, "SAR imaging of suicide bombers wearing concealed explosive threats," Prog. Electromagnetics Res. **125**, 255–272 (2012).
9. M. Elsdon, O. Yurduseven, and D. Smith, "Early stage breast cancer detection using indirect microwave holography," Prog. Electromagnetics Res. **143**, 405–419 (2013).
10. R. K. Amineh, J. McCombe, and N. K. Nikolova, "Microwave holographic imaging using the antenna phaseless radiation pattern," IEEE Antennas Wirel. Propag. Lett. **11**, 1529–1532 (2012).
11. J. Laviada, A. Arboleya-Arboleya, Y. Alvarez-Lopez, C. Garcia-Gonzalez, and F. Las-Heras, "Phaseless synthetic aperture radar with efficient sampling for broadband near-field imaging: theory and validation," IEEE Trans. Antenn. Propag. **63**(2), 573–584 (2015).
12. O. Yurduseven, "Indirect microwave holographic imaging of concealed ordnance for airport security imaging systems," Prog. Electromagnetics Res. **146**, 7–13 (2014).
13. D. M. Sheen, D. L. McMakin, and T. E. Hall, "Three-dimensional millimeter-wave imaging for concealed weapon detection," IEEE Trans. Microw. Theory Tech. **49**(9), 1581–1592 (2001).
14. D. Smith, O. Yurduseven, B. Livingstone, and V. Schejbal, "Microwave imaging using indirect holographic techniques," IEEE Antennas Propag. Mag. **56**(1), 104–117 (2014).

#258155 Received 26 Jan 2016; revised 26 Mar 2016; accepted 26 Mar 2016; published 14 Apr 2016

15. T. S. Ralston, G. L. Charvat, and J. E. Peabody, "Real-time Through-wall imaging using an ultrawideband multiple-input multiple-output (MIMO) phased array radar system," *IEEE International Symposium on Phased Array Systems and Technology*, 551–558 (2010).
16. B. H. Ku, P. Schmalenberg, O. Inac, O. D. Gurbuz, J. S. Lee, K. Shiozaki, and G. M. Rebeiz, "A 77–81-GHz 16-element phased-array receiver with ±50° beam scanning for advanced automotive radars," IEEE Trans. Microw. Theory Tech. **62**(11), 2823–2832 (2014).
17. S. Withington, G. Saklatvala, and M. P. Hobson, "Partially coherent analysis of imaging and interferometric phased arrays: noise, correlations, and fluctuations," J. Opt. Soc. Am. A **23**(6), 1340–1348 (2006).
18. G. L. Charvat, L. C. Kempel, E. J. Rothwell, and C. M. Coleman, "An ultrawideband (UWB) switched-antenna-array radar imaging system," *IEEE International Symposium on Phased Array Systems and Technology*, 543–550, (2010).
19. A. J. Fenn, D. H. Temme, W. P. Delaney, and W. E. Courtney, "The development of phased array radar technology," Linc. Lab. J. **12**(2), 321–340 (2000).
20. D. Shrekenhamer, C. M. Watts, and W. J. Padilla, "Terahertz single pixel imaging with an optically controlled dynamic spatial light modulator," Opt. Express **21**(10), 12507–12518 (2013).
21. D. J. Brady, K. Choi, D. L. Marks, R. Horisaki, and S. Lim, "Compressive holography," Opt. Express **17**(15), 13040–13049 (2009).
22. D. Shin, A. Kirmani, V. K. Goyal, and J. H. Shapiro, "Photon-efficient computational 3-D and reflectivity imaging with single-photon detectors," IEEE Trans. Comput. Imag. **1**(2), 112–125 (2015).
23. O. S. Cossairt, D. Miau, and S. K. Nayar, "Scaling law for computational imaging using spherical optics," J. Opt. Soc. Am. A **28**(12), 2540–2553 (2011).
24. M. F. Duarte, M. A. Davenport, D. Takhar, J. N. Laska, T. Sun, K. F. Kelly, and R. G. Baraniuk, "Single-pixel imaging via compressive sampling," IEEE Signal Process. Mag. **25**(2), 83–91 (2008).
25. D. J. Brady, *Optical Imaging and Spectroscopy* (Wiley, 2009).
26. D. H. Shin, C. W. Tan, B. G. Lee, J. J. Lee, and E. S. Kim, "Resolution-enhanced three-dimensional image reconstruction by use of smart pixel mapping in computational integral imaging," Appl. Opt. **47**(35), 6656–6665 (2008).
27. S. S. Welsh, M. P. Edgar, R. Bowman, P. Jonathan, B. Sun, and M. J. Padgett, "Fast full-color computational imaging with single-pixel detectors," Opt. Express **21**(20), 23068–23074 (2013).
28. J. A. Martinez-Lorenzo, J. H. Juesas, and W. Blackwell, "A single-transceiver compressive reflector antenna for high-sensing-capacity imaging," IEEE Antennas Wirel. Propag. Lett. **15**, 968–971 (2015).
29. J. Hunt, T. Driscoll, A. Mrozack, G. Lipworth, M. Reynolds, D. Brady, and D. R. Smith, "Metamaterial apertures for computational imaging," Science **339**(6117), 310–313 (2013).
30. G. Lipworth, A. Mrozack, J. Hunt, D. L. Marks, T. Driscoll, D. Brady, and D. R. Smith, "Metamaterial apertures for coherent computational imaging on the physical layer," J. Opt. Soc. Am. A **30**(8), 1603–1612 (2013).
31. J. Hunt, J. Gollub, T. Driscoll, G. Lipworth, A. Mrozack, M. S. Reynolds, D. J. Brady, and D. R. Smith, "Metamaterial microwave holographic imaging system," J. Opt. Soc. Am. A **31**(10), 2109–2119 (2014).
32. O. Yurduseven, M. F. Imani, H. Odabasi, J. Gollub, G. Lipworth, A. Rose, and D. R. Smith, "Resolution of the frequency diverse metamaterial aperture imager," Prog. Electromagnetics Res. **150**, 97–107 (2015).
33. T. Fromenteze, O. Yurduseven, M. F. Imani, J. Gollub, C. Decroze, D. Carsenat, and D. R. Smith, "Computational imaging using a mode-mixing cavity at microwave frequencies," Appl. Phys. Lett. **106**(19), 194104 (2015).
34. O. Yurduseven, V. R. Gowda, J. Gollub, and D. R. Smith, "Printed Aperiodic Cavity for Computational Microwave Imaging," IEEE Microw. Wirel. Comp. Lett. (in production) (2016).
35. D. L. Marks, J. Gollub, and D. R. Smith, "Spatially resolving antenna arrays using frequency diversity," J. Opt. Soc. Am. A (in production) (2016).
36. R. T. Hoctor and S. A. Kassam, "The unifying role of the coarray in aperture synthesis for coherent and incoherent imaging," Proc. IEEE **78**(4), 735–752 (1990).
37. S. S. Ahmed, *Electronic Microwave Imaging with Planar Multistatic Arrays* (Logos Verlag Berlin GmbH, 2014).
38. W. M. Siebert, *Circuits, Signals, and Systems* (Massachusetts Institute of Technology, 1985).
39. G. Lipworth, A. Rose, O. Yurduseven, V. R. Gowda, M. F. Imani, H. Odabasi, P. Trofatter, J. Gollub, and D. R. Smith, "Comprehensive simulation platform for a metamaterial imaging system," Appl. Opt. **54**(31), 9343–9353 (2015).
40. Q. Fang, P. M. Meaney, and K. D. Paulsen, "Singular value analysis of the Jacobian matrix in microwave image reconstruction," IEEE Trans. Antenn. Propag. **54**(8), 2371–2380 (2006).
41. M. Pastorino, *Microwave Imaging* (Wiley, 2010).

1. Introduction

The use of microwaves and millimeter-waves for imaging has long been a subject of considerable interest, since electromagnetic waves in these frequency bands are non-ionizing and thus safe for applications such as security screening and biomedical imaging. Moreover, many materials in the radio-frequency (RF) regime are transparent or weakly scattering, thus allowing RF waves to visualize concealed objects, for example those behind walls or under clothes. The majority of active illumination, coherent RF imaging systems are variants on

#258155 Received 26 Jan 2016; revised 26 Mar 2016; accepted 26 Mar 2016; published 14 Apr 2016

either beam scanning or synthetic aperture radar (SAR). In SAR, field measurements are made over a large area, effectively synthesizing a large aperture [1–14]; alternatively, an aperture consisting of an array of sources can be used to create a focused beam that can then be scanned over an object. Phased arrays and active electronically scanned antennas are common examples of beam forming and scanning systems [15–19]. Both methods sample data at the Nyquist limit, with measurements that are essentially orthogonal in the spatial (beam scanning) or Fourier (SAR) domains. Although good image fidelity can be achieved, these methods often have limited imaging speed in the case of SAR, and high cost and system complexity in the case of phased arrays.

All-electronic imaging of objects without using raster scanning and active electronic components can significantly reduce the required imaging time and simplify the system architecture. As the performance and capabilities of modern computing have advanced, computational imaging approaches have gained favor as a means of reducing the constraints associated with the RF system hardware and physical aperture. In essence, computational imaging schemes shift the burden of image reconstruction from physical hardware to processing; as a result, much more flexible and innovative apertures can be used for imaging, with the image estimation procedure becoming more akin to an optimization problem. With computational imaging systems, the radiation (or mode) characteristics of the aperture must be known in detail, along with the introduction of a scattering model for the object. Together, the illumination pattern combined with the scattering model and receive pattern form the system's *forward model*. Unusual and non-traditional apertures can be used for computational imaging schemes, as long as the forward model for the system can be computed or measured [20–28].

Within the context of computational imaging, the frequency-diverse aperture provides an interesting alternative approach to the generation of diverse measurement modes [29–34]. If the aperture is intentionally designed to be frequency dispersive such that the spatial distribution of the aperture fields varies strongly as a function of frequency, then complex field patterns will in turn be radiated as a function of frequency. The scene can thus be interrogated from a passive aperture with numerous distinct measurements using a simple frequency sweep; as the frequency is swept over the operating frequency band, the frequency-dependent complex radiation patterns produced by the aperture encode the scene information, enabling the scene to be reconstructed using computational imaging algorithms. Within this framework, computational imaging systems have been demonstrated involving the use of frequency-diverse metamaterial apertures [29–32] and cavity apertures [33,34]. Metamaterial apertures consist of sub-wavelength resonators patterned into the upper conductor of a double-clad printed dielectric circuit board (PCB). The PCB configuration is equivalent to a parallel-plate waveguide, supporting a guided wave that excites the resonators. The resonance frequencies of the metamaterial elements are randomly distributed over the operating frequency band. As the frequency is swept over the band, those elements whose resonance frequencies coincide with the excitation frequency couple to the guided mode inside the waveguide and radiate into free-space, resulting in complex radiation patterns that vary across the operating frequency band. The number of available measurement modes achieved by this approach is statistically related to the quality (Q-) factor of the resonant elements; for higher Q-factors, more measurement modes are available within the given operating frequency bandwidth.

An alternative approach to achieving a frequency diverse aperture is to increase the dispersion associated with the waveguide excitation mode. An example of this approach is the chaotic cavity imager, recently presented [33]. A version of the chaotic cavity imager consists of three-dimensional (3D) printed, air-filled cavity with a multi-wavelength thickness that allows multi-mode operation. Guided modes within the cavity are mixed in a chaotic manner, so that the excitation field rapidly disperses with frequency. Since the excitation mode varies rapidly with frequency, simple, non-resonant irises patterned into the cavity suffice to couple radiation out forming the desired measurement modes. Since the air-filled cavity has no dielectric losses, and the non-resonant irises have only radiative losses, the air-filled chaotic

#258155 Received 26 Jan 2016; revised 26 Mar 2016; accepted 26 Mar 2016; published 14 Apr 2016

cavity presents a significantly higher Q-factor (and therefore mode-diversity) in comparison to the metamaterial apertures. However, due to its chaotic multi-mode operation, predictive modeling of the air-filled mode-mixing cavity can be a challenging task, increasing the difficulty of obtaining a reliable forward model for image reconstruction. In addition, due to its multi-wavelength thickness, the mode-mixing cavity is not suitable for use in imaging applications where a low-profile aperture is preferred.

The chaotic, air-filled cavity aperture and the metamaterial aperture are two examples of non-traditional imaging configurations that take advantage of computational imaging, and that possess relative strengths and weaknesses. A hybrid version of these configurations has been developed, consisting of a PCB based cavity consisting of a dielectric substrate roughly a half-wavelength in thickness, with non-resonant radiating circular irises forming the aperture [34]. Distinct from the air-filled mode-mixing cavity, the printed cavity operates with a single mode parallel to the radiation direction, with its irises distributed in a non-periodic Fibonacci pattern to randomize the projection of the radiated fields within the imaging domain. Similar to the prior frequency-diverse apertures, the radiating irises of the printed cavity are distributed across the full-aperture, resulting in overlapping sampling of the Fourier components as the imaging frequency is swept, collecting redundant information from the imaging scene.

The transmitting and receiving apertures used in a frequency-diverse imaging system should satisfy certain criteria in order to leverage the computational imaging concept to the full extend. It is desirable in a frequency-diverse imaging system that the transmitting and receiving apertures maximize the spatial coverage (effective aperture) pattern. This enables the aperture pair to maximize the sampled Fourier components, extending the Fourier domain (k-space) support, which is required to optimize the imaging resolution. Moreover, it is also important to reduce the sampling redundancy of the Fourier components, minimizing the correlation of the information collected from the imaging scene as a function of frequency. Minimization of the sampling redundancy can be achieved by choosing optimum aperture patterns producing non-overlapping radiated fields within the imaging domain. Using frequency-diverse apertures with the radiating elements distributed across the full-aperture, such as the metamaterial [29–32] and cavity apertures [33,34], brings three disadvantages; first, a poor effective aperture pattern, second, redundant sampling of the Fourier components, and third, a reduced Q-factor. Since the Q-factor statistically determines the orthogonality of the frequency measurement modes, the aperture should be optimized to minimize the number of radiating elements while maximizing the k-space support [35].

In this paper, we demonstrate an imaging system consisting of planar cavity apertures with sparse complementary radiating irises forming a Mills-Cross pattern for a given transmitting and receiving aperture pair. As a result of employing the Mills-Cross distribution for the radiating irises, the effective aperture is optimized, maximizing the number of the frequency components sampled in the k-space while reducing the sampling redundancy. Moreover, the mode diversity is significantly improved in comparison to the frequency-diverse apertures consisting of radiating elements distributed across the full-aperture. This paper is organized as follows. In section 2, the concept of frequency-diverse image reconstruction is briefly explained. In section 3, we demonstrate the design of the Mills-Cross cavity apertures. This section covers the optimization of the radiating elements, investigation of the effective aperture concept and the sampling of the k-space. It also demonstrates the analysis of the mode-orthogonality for the proposed Mills-Cross cavity apertures through singular value decomposition (SVD), and assessment of the mode-diversity and the radiation efficiency performance of these apertures for computational imaging applications. In section 4, we show an experimental imaging system for the imaging of a number of targets. Finally, section 5 provides concluding remarks.

2. Frequency-diverse computational imaging and image reconstruction

As with any computational imaging system, it is essential to determine a forward model that provides a description—exact as possible—of the radiated field pattern from the aperture, as

#258155 Received 26 Jan 2016; revised 26 Mar 2016; accepted 26 Mar 2016; published 14 Apr 2016

well as the scattering from objects in the scene. At RF wavelengths, humans as well as many objects and structures of interest are partially conductive and can be reasonably approximated as metallic scatterers. Thus, we can model the scene by discretizing it into a set of 3D voxels, each voxel represented by an isotropic susceptibility that relates the local incident field to the scattered field. Making the approximation that the incident field from the aperture is unperturbed by scattering from the scene (first Born approximation) vastly simplifies the forward model and allows the measurement matrix to be computed rapidly [30]. A measurement of the scene consists of the signal reflected from the object of interest (amplitude and phase); the collection of these signals over the operating frequency band comprise the measurement vector, **g**. Since the number of measurements is limited by the cavity Q factor, and the number of scene sampling points is limited by the system resolution, the imaging problem reduces to a finite dimension matrix equation that relates the measurements to the reflectivity values of the scene, **f**, according to

$$\mathbf{g}_{Mx1} = \mathbf{H}_{MxN}\mathbf{f}_{Nx1} \tag{1}$$

In Eq. (1), M is the total number of measurements while N denotes the number of voxels into which the imaging scene is discretized. Ideally, the number of measurements would be equal to or greater than the number of reflectivity values to be reconstructed; however, finite Q-factors tend to limit the number of measurement modes available through frequency diversity. In addition, the typical mode patterns that result from the frequency diverse aperture tend to exhibit some degree of correlation, so that the effective number of modes can even be less than that calculated by dividing the bandwidth by the resonance bandwidth. For computational imaging systems like the frequency-diverse aperture considered here, correlations of the modes allow the data to be undersampled, reducing both the data acquisition and computational burden. The optimum number of measurements and optimal field patterns is dependent on the details of the system and the types of objects to be imaged.

H in Eq. (1) is the measurement matrix. Within the first Born approximation, the element of **H** that relates the reflectivity value at a given position to a measurement is proportional to the pointwise product of the fields radiated by the transmitting, $\mathbf{E}_{\mathbf{Tx}}$, and receiving, $\mathbf{E}_{\mathbf{Rx}}$, frequency-diverse apertures, or $\mathbf{H} \propto \mathbf{E}_{\mathbf{Tx}}\mathbf{E}_{\mathbf{Rx}}$, where the fields are evaluated at the position of the reflectivity value. Reconstructing the scene reflectivity (or contrast) vector, **f**, in Eq. (1) thus constitutes an inverse problem. Investigating Eq. (1), it can be seen that the measurement matrix **H** is not full-rank, $M \neq N$, (ill-conditioned) and therefore does not have an exact inverse. Many reconstruction techniques can be applied to estimate the reflectivity vector that range from straightforward (e.g., matched filter, pseudo-inverse) to sophisticated (e.g., compressive techniques, such as least-squares and TwIST + TV) [32]. The more advanced techniques can make use of prior information to arrive at a better estimation of the scene, but generally require iterative refinement making them slower. For the reconstructions presented here, we use matched filter reconstruction as it requires no matrix inverse and allows for fast reconstructions. Using the matched-filter technique, we reconstruct the imaging scene, $\mathbf{f}_{\mathbf{recon}}$, as follows [32]:

$$\mathbf{f}_{\mathbf{recon}} = \mathbf{H}^{\dagger}\mathbf{g} \tag{2}$$

In Eq. (2), $\mathbf{H}^{\dagger}$ is the conjugate (or Hermitian) transpose of the measurement matrix, **H**.

3. Planar Mills-Cross cavity apertures

Aperture optimization is an important aspect of designing an imaging system [36]. Given that the number of measurement modes for a frequency-diverse aperture is limited by the Q-factor, it is important that the information content within those modes be maximized as much as possible, which can be achieved generally by making the field patterns of the measurement modes as orthogonal as possible in some basis. With the design of the PCB cavity assumed as fixed, the degree of freedom available for optimizing the field patterns is the number and arrangement of the radiating irises over the aperture, as well as the aperture layout. The

#258155 Received 26 Jan 2016; revised 26 Mar 2016; accepted 26 Mar 2016; published 14 Apr 2016

design approach followed here is to maximize the sampling of the k-space components, accessing as many components as possible while minimizing mode sampling overlap.

Since the measurement matrix elements are proportional to the product of the fields from the transmit and receive apertures, the Fourier space sampled by the combination is jointly determined by the arrangement of irises on both the transmit and receive apertures. Ideally, the fields radiated by the receiving and transmitting apertures should sample different (non-overlapping) sub-sets of k-space, ensuring the non-redundant sampling of the Fourier components. Redundant sampling reduces the information content of the measurement modes sampling the imaging scene and therefore needs to be avoided [35].

The k-space analysis can be simplified under cirtain conditions. For the sake of simplicity, assume that two apertures are placed in the spatial-domain, transmitting and receiving, with linearly-oriented radiating elements as shown in Fig. 1. As an example, each array contains three radiating irises. As shown in Fig. 1(a), if the apertures are far away from the imaging domain, $k_0 |\mathbf{r}| >> 1$, the vectors denoting the Fourier components between the points and the imaging domain, $\mathbf{r}$, are nearly parallel. When Fourier transformed, these points from the transmit and receive irises are projected onto their respective k-spaces reflected over the origin as depicted in Fig. 1(b). The 3D convolution of their projections in the k-space are placed in a k-space that is approximately a sphere double the radius of the transmit and receive k-spheres. As shown in Fig. 1(c), as the transmit and receive Fourier components occupy only a small region of the sphere that is approximately a section of a plane, the convolution of these two sections is likewise a plane. Alternatively, for the given case, we can convolve these discrete points in the spatial domain as shown in Fig. 1(a). Investigating Figs. 1(a)-1(c), it can be seen that under the far-field condition, the projection of the convolved components on the k-space sphere to a 2D plane produces a similar pattern to the convolution of the selected discrete points in the spatial domain.

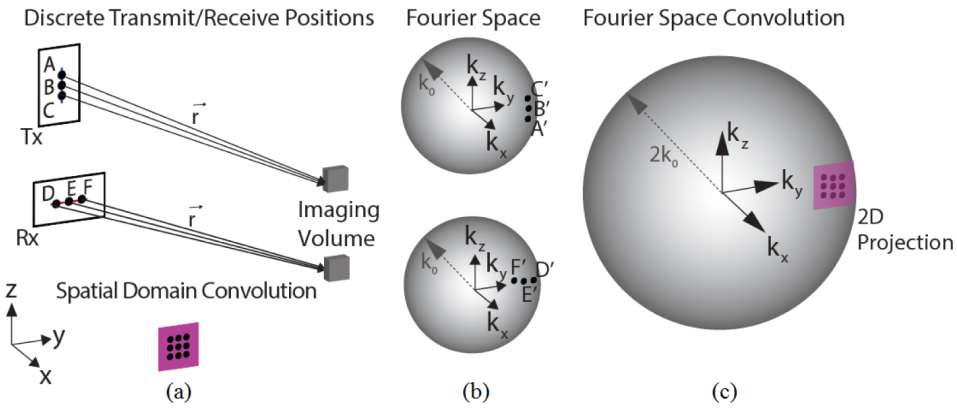

Fig. 1. Spatial and k-space analysis of two apertures - $k_0 |\mathbf{r}| >> 1$ (a) apertures with discrete transmit and receiving points, and their convolution in the spatial domain (b) projections of the discrete points onto k-spheres in the Fourier domain (c) convolution in the Fourier domain and projection onto a 2D plane. Rx and Tx denote receiving and transmitting, respectively.

This suggests that the convolution of the fields at the aperture planes in the spatial domain provides a good estimation for analyzing the sampling provided by these apertures in the k-space. It should be mentioned here that this assumption approximately holds in the close range case (Fresnel region), and exhibits a reliable approach for the optimization of the aperture distribution to optimize the k-space sampling in imaging applications.

We analyzed various aperture structures with different radiating iris arrangements with the goal of maximizing diversity in k-space, including periodic, aperiodic, diagonal, square, circular and Mills-Cross configurations as shown in Fig. 2.

#258155 Received 26 Jan 2016; revised 26 Mar 2016; accepted 26 Mar 2016; published 14 Apr 2016

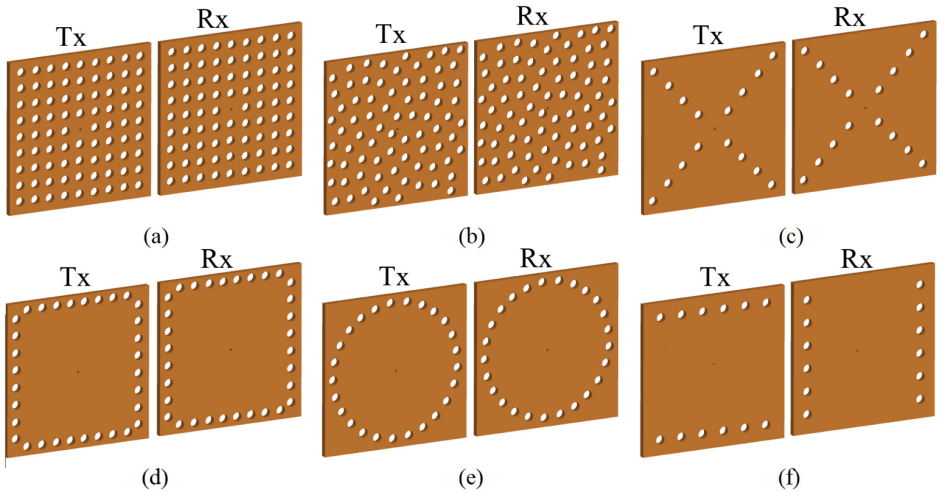

Fig. 2. Some iris configurations analyzed for the optimization of the effective aperture and k-space sampling (a) periodic (b) aperiodic (c) diagonal (d) rectangular (e) circular (f) Mills-Cross.

For this analysis, the irises were assumed to be excited with fields having identical amplitude and phase distributions. The fields at the aperture planes of the transmitting and receiving apertures were convolved with each other to obtain the coverage pattern in the spatial domain, which also indicates the effective aperture produced by the corresponding apertures when employed in an imaging system [37]. As a result of this study, the Mills-Cross iris distribution was found to produce the optimum coverage pattern. Figure 3 below illustrates the Mills-Cross iris distribution for the transmitting and receiving apertures together with the effective aperture pattern produced by this transmitting / receiving aperture pair. In Fig. 3, the receiving and transmitting apertures have 12 irises, placed along two horizontal rows and vertical columns, 2 x 6, respectively. In order to calculate the effective aperture pattern in Fig. 3(c), the power patterns at the aperture plane of the transmitting and receiving apertures are convolved in the spatial domain as follows:

$$\mathbf{A}_{\text{eff}} = \sum_{i=-y'}^{y'} \sum_{j=-z'}^{z'} \mathbf{E}_{\mathbf{AT}_x}(i,j)\mathbf{E}_{\mathbf{AR}_x}(y-i,z-j) \tag{3}$$

In Eq. (3), the apertures are assumed to lie in the yz-plane. $\mathbf{E}_{\mathbf{ATx}}$ and $\mathbf{E}_{\mathbf{ARx}}$ denote the field distributions (power) at the transmiting and receiving aperture planes, respectively.

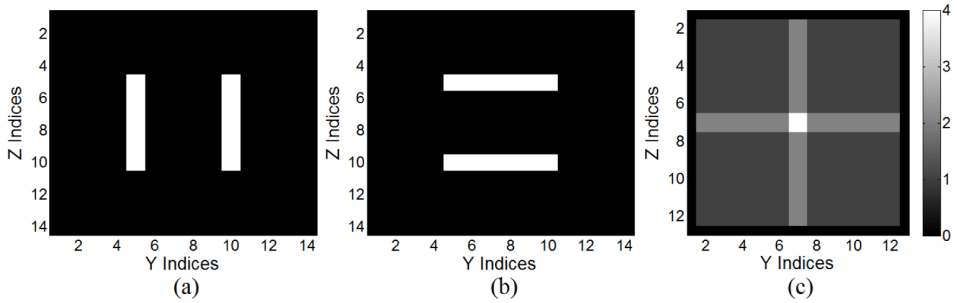

Fig. 3. Optimized radiating iris patterns for the receiving and transmitting apertures (a) receiving pattern (b) transmitting pattern (c) coverage pattern in the spatial domain (effective aperture).

The convolution pattern in Fig. 3(c) provides a good means of assessing the sampling of the Fourier components in the k-space. The color bar in Fig. 3(c) indicates the number of

#258155 Received 26 Jan 2016; revised 26 Mar 2016; accepted 26 Mar 2016; published 14 Apr 2016

times each Fourier component is sampled, with the total number of sampled components corresponding to the maximum number of independent measurements (absent any correlation). In Fig. 3(c), 100 components are sampled once (no redundancy), 20 components are sampled twice, and one component is sampled four times. In total, there are 121 Fourier components sampled. Given that the transmitting and receiving apertures have 12 irises, N_{Tx} = 12 and N_{Rx} = 12, the maximum number of spatial modes supported by a single transmitting / receiving aperture pair is 144, which is consistent with the upper-bound limit for the sampled Fourier components.

An important study for the design of the Mills-Cross apertures is the optimization of the radiating irises, which involves two steps; first, determining the size of the radiating irises, and second, determining the number of the irises. The effective radiating iris dimension is inversely proportional to the overall Q-factor of a loaded cavity due to the increased radiation loss by a factor of r^3, where r is the iris diameter [35]; thus, increasing the diameters or the number of radiating irises, while adding mode diversity, lowers the Q-factor of the aperture. Therefore, when optimizing the iris dimension for the Mills-Cross apertures, two important criteria must be considered; Q-factor and radiation efficiency. Based on the parametric analysis performed using a 3D full-wave electromagnetic simulator, CST Microwave Studio, the size of the radiating irises for the Mills-Cross apertures demonstrated in this work was chosen to be 5 mm (diameter). The number of radiating irises on a selected transmitting / receiving aperture pair sets a limit on the number of supported measurement modes according to [35]:

$$Q = \frac{N_{Tx} N_{Rx} f_0}{B} \tag{4}$$

In Eq. (4), N_{Tx} and N_{Rx} denote the number of radiating irises on the transmitting and receiving apertures, respectively, while f_0 is the central imaging frequency, f_0 = 22 GHz, and B is the imaging bandwidth, B = 9 GHz. Equation (4) provides a good estimate of the optimum number of radiating irises with respect to the Q-factor of a frequency-diverse aperture. Increasing the number of irises beyond this limit results in the aperture producing more mode combinations than it can optimally support, introducing redundant information. In addition, each additional iris introduced in the apertures reduces the Q-factor. A study was thus performed to optimize the Q-factor / iris number ratio, with the optimum response achieved when Q = 230 and $N_{Tx} = N_{Rx}$ = 12.

With the number of irises determined, the Mills-Cross cavity apertures were fabricated on double-sided copper-clad Rogers 4003 substrate, ε_r = 3.55 and tanδ = 0.0027. The irises are patterned onto the front surface while the rear surface of the cavity serves as ground plane for the planar waveguide. The fabricated apertures are shown in Figs. 4(a) and 4(b) while Fig. 4(c) demonstrates a schematic for the Mills-Cross apertures.

#258155 Received 26 Jan 2016; revised 26 Mar 2016; accepted 26 Mar 2016; published 14 Apr 2016

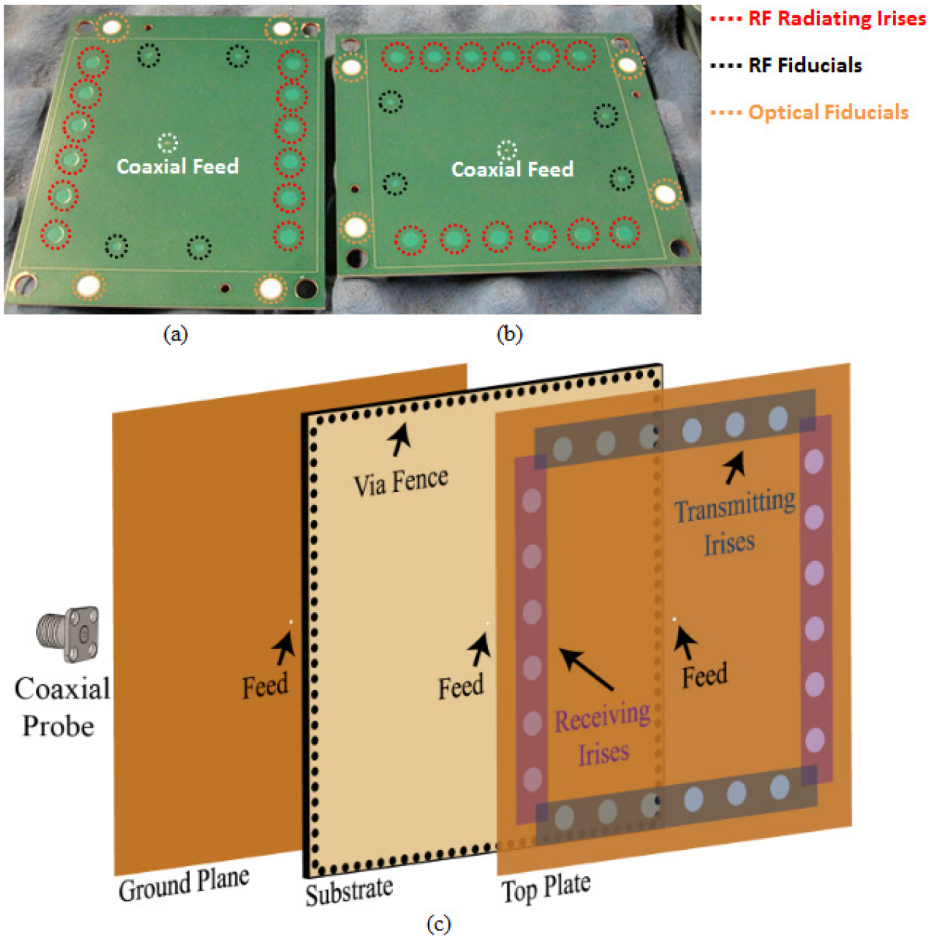

Fig. 4. Fabricated Mills-Cross cavity apertures (a) receiving aperture (b) transmitting aperture (c) schematic of the Mills-Cross antennas (inside the via fence region). Receiving irises are for the receiving aperture while the transmitting irises are for the transmitting aperture.

As can be seen in Fig. 4, each Mills-Cross cavity aperture consist of an array of twelve radiating, non-resonant circular irises printed on the front surface of the cavity aperture. Similar to the arrangement of the irises depicted in Fig. 3, the receive aperture has its irises vertically oriented while the transmitting aperture has horizontally oriented irises arranged in a linear array. To contain the TEM cavity modes and form the edges of the cavity structure, a via fence wall is introduced along the edges of the PCB board. A close inspection of Fig. 4 reveals four additional irises within the via fence region, which are smaller in size (3.5 mm diameter) in comparison to the radiating irises along the edges. It can also be seen that outside the via fence region, there are four optical fiducials. These RF and optical fiducial alignment irises are used to orient, position and locate the Mills-Cross cavities within the collective aperture as will be briefly explained in section 4.

The green coating one the apertures shown in Figs. 4(a) and 4(b) is a solder mask coating used to prevent oxidization of the copper PCB. The solder mask has a thickness of $t = 17\mu m$, which is smaller than $\lambda_g/10$ over the K-band, where λ_g is the guided wavelength within the dielectric substrate. Given the electrically small thickness combined with non-resonant response of the radiating circular irises, the solder mask has a negligible effect on the RF response of the apertures.

#258155 Received 26 Jan 2016; revised 26 Mar 2016; accepted 26 Mar 2016; published 14 Apr 2016

To assess the performance of the Mills-Cross cavity apertures for computational imaging applications, the Q-factor and the radiation efficiency of the apertures must be analyzed. The Q-factor of a cavity can be determined by observing the exponential decay of a transient RF excitation in the time-domain [38]. To obtain values of the Q-factor for the fabricated apertures, we used a vector network analyzer (VNA), Agilent N5245A, and measured the voltage impulse response in the time-domain as shown in Fig. 5.

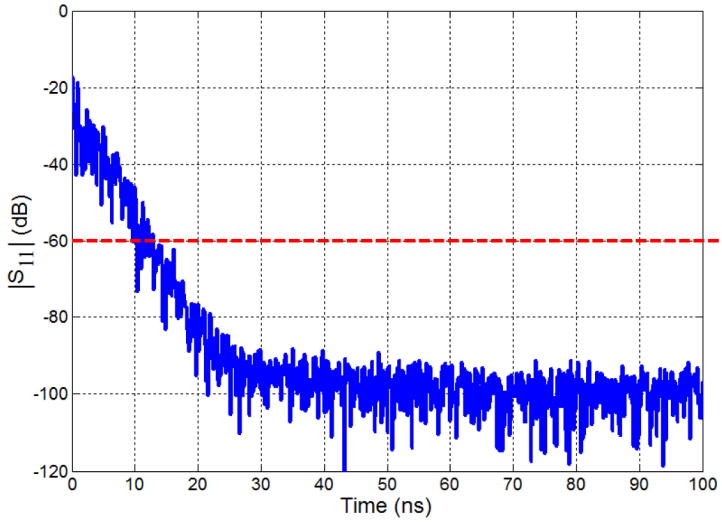

Fig. 5. Time-domain impulse response of the Mills-Cross cavity apertures.

In Fig. 5, a level of −60 dB is selected as a threshold for the decay of the impulse response for two reasons; first, above this threshold limit, the impulse decay response can be approximated as a linear curve on the log-linear plot, making it possible to calculate the signal decay factor, α in $e^{-\alpha t}$. Second, the −60 dB threshold level is above the noise floor of the VNA (oscillating around −100 dB), eliminating the risk of the windowed region being distorted by additional noise factors. Under these circumstances, the following equation is used to calculate the Q-factor of the apertures.

$$Q = \frac{2\pi f}{2\alpha} \tag{5}$$

In Eq. (5), f is the frequency at which the Q-factor is calculated. Using Eq. (5), the Q-factor of the Mills-Cross apertures was determined across 101 frequencies over the K-band and the averaged Q-factor was calculated to be Q_{av}≈230. To put this value into context, we should compare the Q-factor response of the Mills-Cross cavity to the prior frequency-diverse apertures we have demonstrated up to date. The metamaterial apertures in [29–32] exhibit a Q-factor of $Q \approx 60$ while the Q-factor of the printed Fibonacci cavity aperture in [34] is Q = 140. This suggests that in comparison to prior systems, we have achieved an increase of 283% and 64.3%, respectively, as a result of adopting the Mills-Cross layout.

The radiation efficiency of the Mills-Cross apertures was measured by scanning the radiated electric field using a NSI planar near-field scanner [39]. The tangential components of the electric field were measured by means of a transmission scan, S_{21}, over a planar surface (yz-plane) discretized into N (y-axis) and M (z-axis) points at the Nyquist sampling limit over the K-band. The scan was performed over a ± 60° field-of-view (FOV), providing sufficient windowing to capture the fields radiated by the apertures. The measured electric field value at each (y,z) sampling point was recorded, S_{21}(y,z) and integrated over the scan FOV using the following equation to calculate the radiation efficiency.

#258155 Received 26 Jan 2016; revised 26 Mar 2016; accepted 26 Mar 2016; published 14 Apr 2016

$$\eta(f)=\sum_{z=1}^{M}\sum_{y=1}^{N}\frac{\left|S_{21}(y,z;f)\right|^2}{1-\left|S_{11}(f)\right|_2^2}\Bigg|_{f:17.5\,GHz\to 26.5\,GHz} \tag{6}$$

In Eq. (6), $\eta(f)$ denotes the efficiency as a function of frequency sweep over the K-band while S_{11} is the reflection coefficient of the apertures. For an aperture providing a good impedance match ($|S_{11}|$<-10 dB), Eq. (6) can be reduced to

$$\eta(f)=\sum_{z=1}^{M}\sum_{y=1}^{N}\left|S_{21}(y,z;f)\right|^2\Bigg|_{f:17.5\,GHz\to 26.5\,GHz} \tag{7}$$

The calculated radiation efficiency pattern of the Mills-Cross apertures is shown in Fig. 6 together with the reflection coefficient, S_{11}, over the K-band. Averaged over the K-band, the Mills-Cross cavity apertures exhibit an average radiation efficiency, η_{av} = 28%.

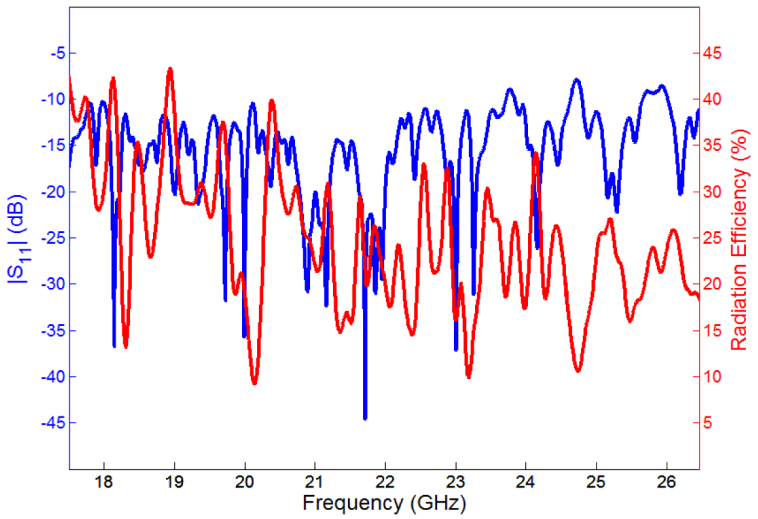

Fig. 6. S_{11} and radiation efficiency patterns of the Mills-Cross cavity apertures as a function of frequency.

For the effective aperture analysis depicted in Fig. 3, it was assumed that the radiating irises of the transmitting and receiving apertures have a uniform amplitude distribution. However, in practice, this assumption does not hold. The coaxial feed of the fabricated Mills-Cross cavity apertures launces a cylindrical-wave inside the substrate (guided-wave), which can be modeled using a Hankel function of the second kind, $H_0^{(2)}$. Therefore, it is important to perform this study using the actual measured fields of the fabricated apertures. It should be emphasized that the Hankel function describes the cylindrical-wave launced by the coaxial probe inside the dielectric substrate of the Mills-Cross cavity apertures. Once the launched wave reaches the edges of the cavity, it undergoes reflections from the via fence wall, which results in the resultant wave propagation diverging from the cylindrical wave assumption. The actual field distribution, at any point, is the summation of all the scattered waveforms generated by the multi-propagation paths in the cavity. In Fig. 7, the normalized power patterns of the Mills-Cross cavity apertures obtained from the measured fields back-propagated to the aperture plane are demonstrated together with the corresponding convolved effective aperture distributions as a function of frequency over the K-band. The convolution patterns are normalized with respect to the most redundant sampled component (highest value in the effective aperture pattern). The results in Figs. 7(a)-7(c) are reported at selected frequencies, 17.5 GHz, 22 GHz and 26.5 GHz, respectively, while Fig. 7(d) shows the overall patterns superposed over the K-band. As can be seen in Figs. 7(a)-7(c), as the frequency is

#258155 Received 26 Jan 2016; revised 26 Mar 2016; accepted 26 Mar 2016; published 14 Apr 2016

swept, the field distribution across the aperture plane varies, resulting in frequency-dependent effective aperture patterns. In Fig. 7(d), all the radiating irises are clearly visible and the fiducial irises (for system alignment) exhibit weaker radiation (due to less coupling to the guided-wave) as a result of having a smaller size. The overall effective aperture pattern in Fig. 7(d) is in good agreement with the analysis illustrated in Fig. 3(c). As shown in Fig. 7(d), the use of the Mills-Cross pattern optimizes the effective aperture, maximizing the number of the Fourier components sampled in k-space while minimizing the sampling redundancy. In comparison to the most redundantly sampled component in the center, the components along the vertical and horizontal lines intersecting in the center are sampled twice less redundantly while the other components are sampled four times less redundantly.

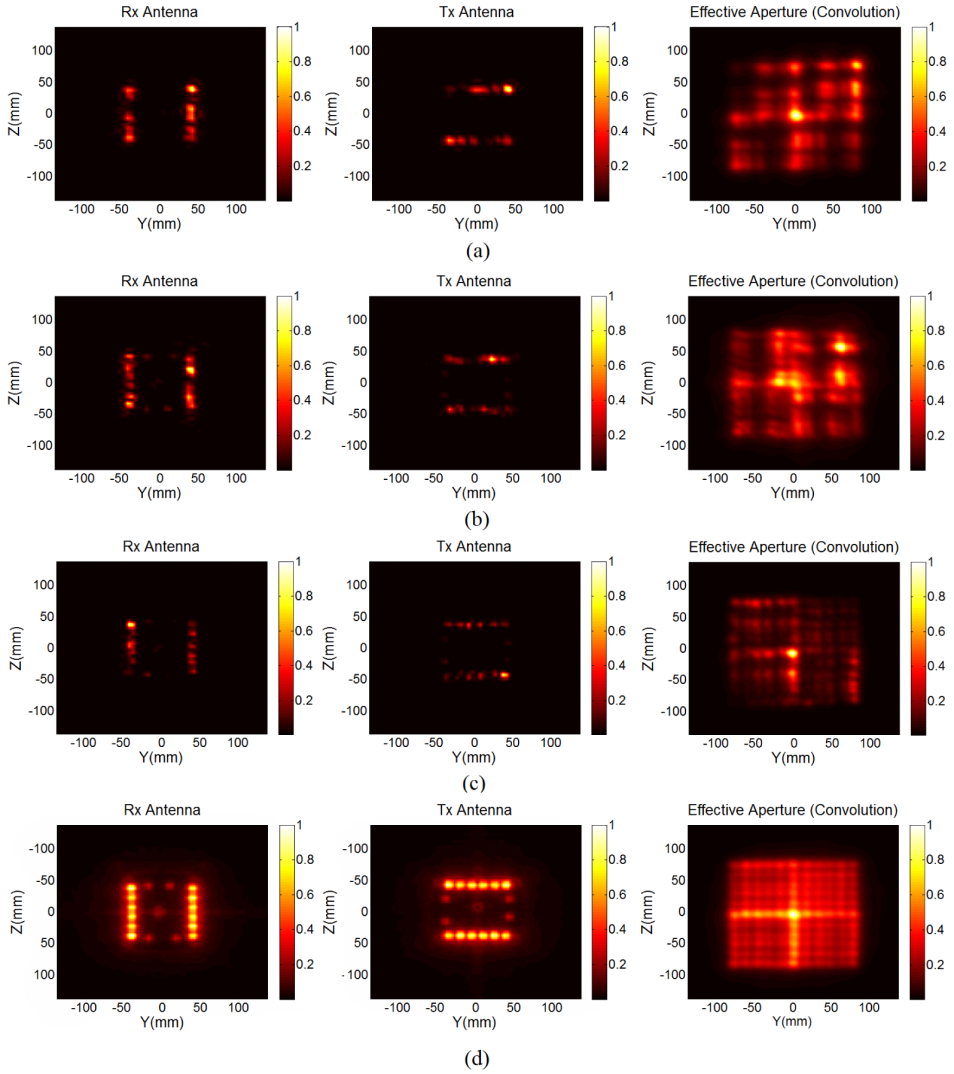

Fig. 7. Back-propagated patterns and effective aperture distributions for the transmitting and receiving Mills-Cross apertures (a) 17.5 GHz (b) 22 GHz (c) 26.5 GHz (d) superposed over the K-band (101 frequency points).

It should be noted that different from the metamaterial apertures in [29–32], the frequency-diversity of the Mills-Cross apertures does not stem from switching the irises on / off as a function of a frequency sweep. While the metamaterial unit cells of the apertures

#258155 Received 26 Jan 2016; revised 26 Mar 2016; accepted 26 Mar 2016; published 14 Apr 2016

reported in [29–32] have a Lorentzian resonance response, the radiating irises of the Mills-Cross apertures couple to the cavity modes across the entire operating frequency band, K-band. However, the excitation cavity waveform at the position of the irises varies as a function of frequency, driving a frequency-dependent radiation response of the irises, as shown in Figs. 7(a)-7(c).

Comparing the Mills-Cross apertures with a non-optimized aperture configuration is important to visualize the improvement in the effective aperture pattern and the sampling redundancy achieved using the proposed Mills-Cross structure. In view of this, we designed another pair of transmitting and receiving apertures with the radiating irises distributed across the full-aperture using the aperiodic pattern shown in Fig. 2(b). Figure 8 below demonstrates the back-propagated fields to the aperture plane together with the convolved effective aperture pattern. Similar to the study demonstrated for the Mills-cross apertures in Fig. 8, the convolution pattern is normalized with respect the most redundant sampled component.

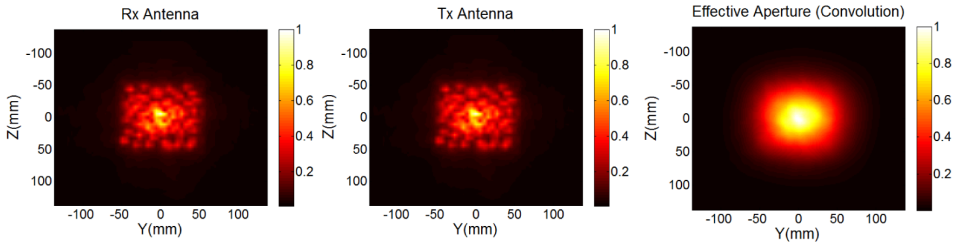

Fig. 8. Back-propagated patterns and effective aperture distributions for the non-optimized apertures with radiating irises distributed across the full-aperture. The patterns are superposed over the K-band (101 frequency points).

Comparing the effective aperture patterns in Fig. 7(d) and Fig. 8 reveals two important outcomes; first, the effective aperture pattern for the non-optimized apertures is smaller, suggesting that the number of the sampled Fourier components is reduced, and second, the sampling redundancy is significantly increased.

As mentioned earlier, the frequency-diverse apertures demonstrated to date have radiating elements distributed across the full-surface of the apertures. For the frequency-diverse metamaterial apertures [29–32], for example, the radiating, resonant metamaterial elements form a dense array over the aperture, with resonance frequencies randomly assigned to each resonator. The air-filled mode-mixing cavity in [33] and its printed single-mode version in [34] have periodic and aperiodic (Fibonacci) iris distributions, respectively, again distributed using the full-aperture. Distinct from these previously reported apertures, the Mills-Cross apertures exhibit a sparse iris pattern, as shown in Fig. 4. In addition to optimizing the k-space sampling, this sparse arrangement brings a number of advantages; first, the analytical modeling of the radiation from the irises is more feasible, as the apertures have a much simpler geometry with only a few radiating elements; second, using the proposed apertures forming a Mills-Cross pattern for any given transmitting / receiving pair (complementary with respect to each other), the correlation between projections of the fields radiated by a pair of transmitting and receiving apertures in the imaging domain is significantly minimized; and third, as the number of the radiating elements is minimized, the proposed Mills-Cross cavity apertures present a superior Q-factor (and therefore mode diversity).

In order to investigate the orthogonality of the measurement modes produced by an aperture as a function of frequency, a singular value decomposition (SVD) analysis can be applied [40,41]. Such an analysis is important as a means of quantifying the improved mode-diversity for the proposed Mills-Cross cavity apertures. To demonstrate the advantages and tradeoffs associated with the various designs, we constructed two-imaging systems, both consisting of two apertures. As can be seen in Fig. 9(a), the first imaging system consists of Fibonacci cavity aperures while the second imaging system in Fig. 9(b) consists of the proposed Mills-Cross cavity apertures working as receiver and transmitter.

#258155 Received 26 Jan 2016; revised 26 Mar 2016; accepted 26 Mar 2016; published 14 Apr 2016

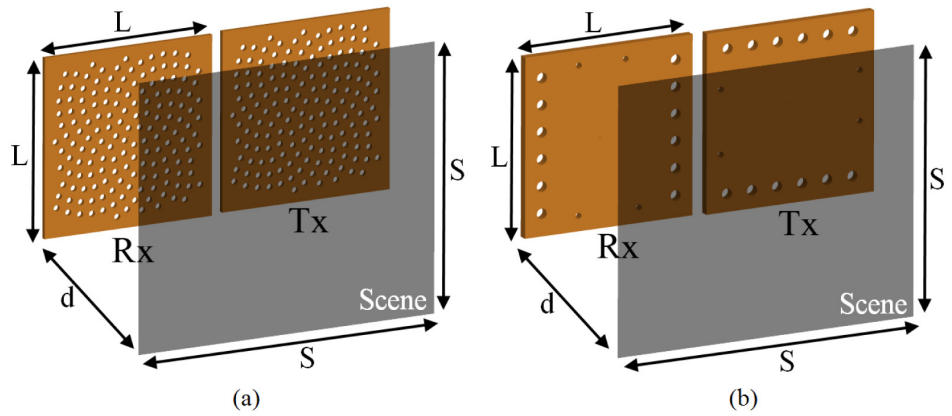

Fig. 9. Imaging systems for SVD analysis (a) Fibonacci cavity apertures (b) Mills-Cross cavity apertures (L = 10 cm, S = 1 m and d = 1 m).

For the SVD analysis, we measured the electric fields radiated by the Fibonacci and Mills-Cross cavity apertures using the NSI near-field scanner over a ± 60° FOV at the Nyquist limit. We then forward-projected these fields to a two-dimensional (2D) scene (1m x 1m) at d = 1m away from the apertures using dyadic Green's functions [30] and calculated the measurement matrix, **H**, corresponding to each configuration. The obtained singular value spectrums corresponding to these systems are shown in Fig. 10.

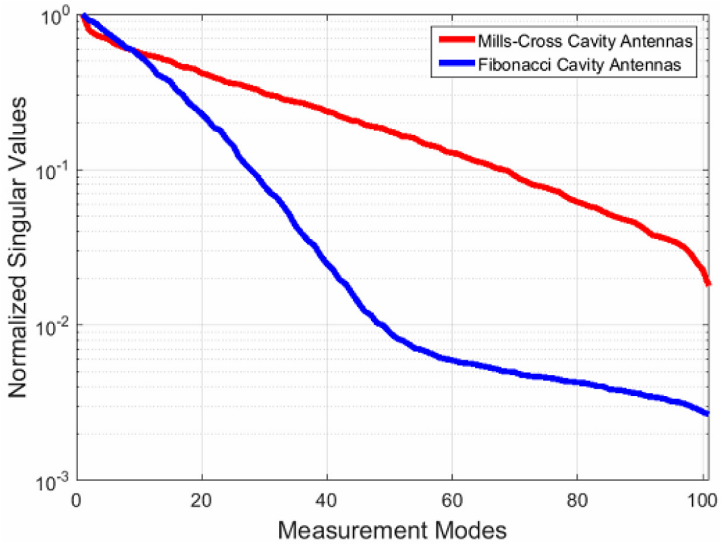

Fig. 10. Comparison between the normalized SVD patterns of Fibonacci and Mills-Cross cavity apertures (log-linear plot).

Figure 10 reveals that the singular value spectrum corresponding to the Mills-Cross cavity aperture falls off much more slowly as a function of increasing mode number than that of the Fibonacci cavity aperture, indicating that the measurement modes of the Mills-Cross aperture have considerably less correlation. To visualize the improvement in mode-diversity, in Fig. 11, we plot the normalized amplitude of the measurement matrix, $|\mathbf{H}|$, at selected frequencies. Comparing the fluctuations in the measurement matrices for the two types of apertures, it is evident from Fig. 11 that the fields produced by the proposed Mills-Cross cavity apertures exhibit substantially more diversity.

#258155 Received 26 Jan 2016; revised 26 Mar 2016; accepted 26 Mar 2016; published 14 Apr 2016

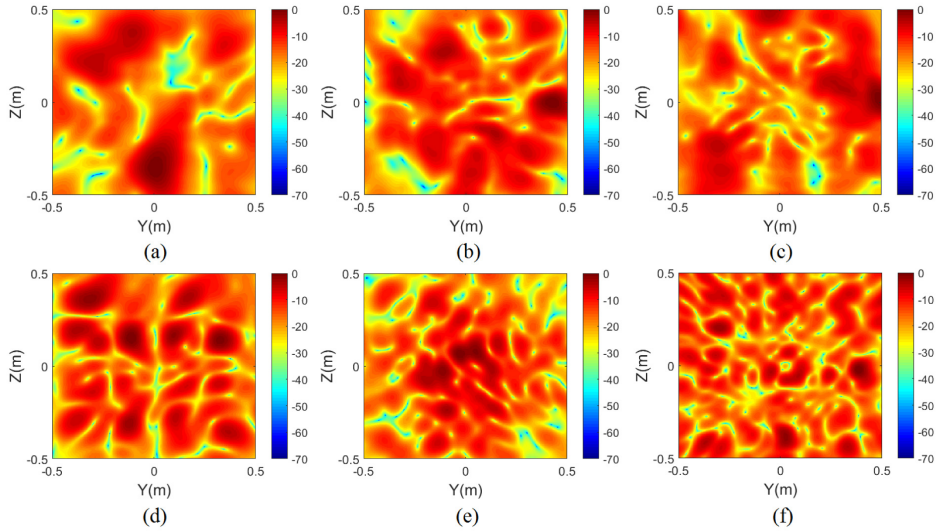

Fig. 11. Normalized amplitude patterns (dB) of the measurement matrix, $|\mathbf{H}|$, at selected frequencies. Fibonacci cavity aperture (a) 17.5 GHz (b) 22 GHz (c) 26.5 GHz; Mills-Cross cavity aperture (d) 17.5 GHz (e) 22 GHz (f) 26.5 GHz.

4. Experimental Mills-Cross imaging system and imaging results

A photograph of the experimental Mills-Cross imaging system is shown in Fig. 12(a), with a depiction of the aperture layout shown in Fig. 12(b). The frequency diverse measurements are taken at 101 frequency points equally spaced over the K-band. As shown in Fig. 12, the Mills-Cross imaging system consists of 6 receiving and 6 transmitting apertures, producing M = 3,636 total number of measurement modes, calculated as *number of transmitting apertures* (6) x *number of receiving apertures* (6) x *number of frequency sampling points* (101). As a result of having an array of transmitting and receiving apertures, the system performs imaging in a multi-static manner. Multistatic operation enables the imaged objects to be viewed from different angles (angular diversity), extending the k-space support provided by the apertures in the Fourier domain. Using multiple apertures also increases the number of measurements modes produced by the system. The transmitting apertures are connected to the first port of the VNA while the receiving apertures are connected to the second port. In order to switch between the apertures, as depicted in Fig. 12(b), two coaxial switches, Keysight L7106C, are used, controlling the transmitting and receiving apertures, respectively. As shown in Fig. 12, the apertures are distributed in an aperiodic pattern. This is due to avoid periodic sampling of the imaging scene to prevent aliasing artifacts in the reconstructed images.

#258155 Received 26 Jan 2016; revised 26 Mar 2016; accepted 26 Mar 2016; published 14 Apr 2016

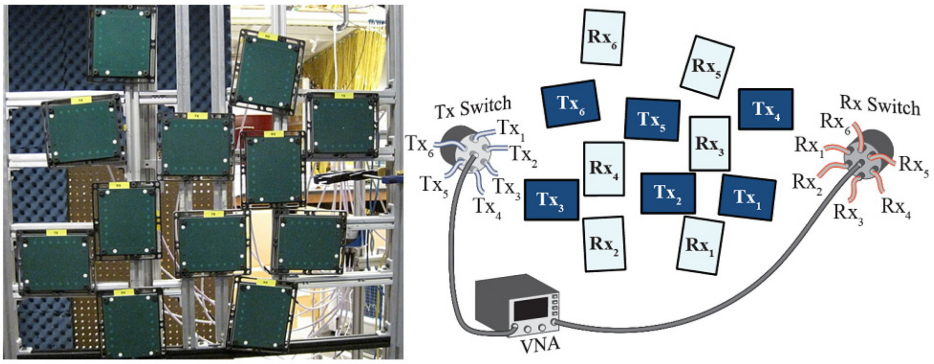

Fig. 12. Mills-Cross imaging system consisting of 12 apertures (6 receiving, Rx, and 6 transmitting, Tx) (a) experimental system set-up (b) imaging system layout (transmitting and receiving apertures are highlighted in dark and light blue colors, respectively).

As mentioned earlier, to achieve the alignment of the apertures within the experimental set-up, we make use of the correlation between a set of RF fiducials and corresponding set of optical fiducials. When we measure the fields of the Mills-Cross apertures (via a near-field scan) and back-propagate these fields to the aperture plane (producing plots such as those shown in Fig. 7, for example), we obtain the locations of the apertures with respect to the aperture centers. We then place the apertures in the experimental set-up and perform an optical scan to determine their positions in space by using an optical scanning system (CREAFORM 3D Laser Scanner). The optical scanner senses only the optical fiducials. After the optical scan of the experimental set-up, we use the vector relationship between the locations of the RF fiducials and the optical fiducials, to put the apertures in their exact positions within the set-up for imaging. Correct alignment of the apertures within the experimental set-up ensures that there is no mismatch between the fields forward-propagated to the imaging scene (calculated using Green's functions on the near-field measured fields), which forms the measurement matrix, **H**, and the actual fields radiated from the apertures illuminating the imaging domain, collecting the measurement vector, **g**, in Eq. (1). Therefore, alignment of the apertures is an important aspect to achieve imaging. Details regarding the position alignment of the apertures will be forthcoming and beyond the scope of this paper.

Following the alignment of the system, imaging of a number of targets, including a resolution target, an L-shaped phantom and a "DUKE" target, was performed using the Mills-Cross imaging system. A depiction of the imaging system for 3D imaging is illustrated in Fig. 13.

#258155 Received 26 Jan 2016; revised 26 Mar 2016; accepted 26 Mar 2016; published 14 Apr 2016

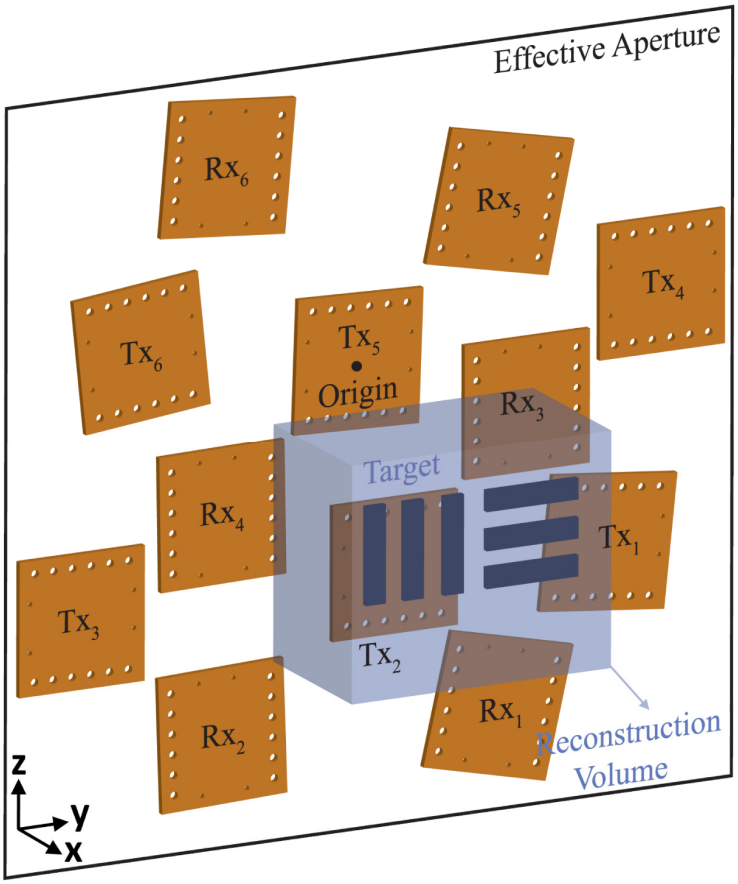

Fig. 13. Depiction of the Mills-Cross imaging system for 3D imaging (not drawn to scale). Resolution target is shown as the imaged object inside the 3D reconstruction volume as an example. Position (y, z) and rotation (minus sign denotes counter-clockwise rotation) of the Mills-Cross apertures in units of meter and degree; Rx_1 = (0.13, –0.33, 6°), Rx_2 = (–0.14, –0.35, –2°), Rx_3 = (0.15, –0.04, 0°), Rx_4 = (–0.13, –0.14, 0°), Rx_5 = (0.13, 0.14, 9°), Rx_6 = (–0.14, 0.19, 3°), Tx_1 = (0.22, –0.18, 2°), Tx_2 = (0.03, –0.18, 0°), Tx_3 = (–0.26, –0.22, 0°), Tx_4 = (0.28, 0.04, 0°), Tx_5 = (0,0, 0.6°), Tx_6 = (–0.2, 0.03, –4°).

The range (δ_r) and cross-range (δ_{cr}) resolutions for the imaging system can be estimated using the standard expressions common in SAR [32], or

$$\delta_r = \frac{c}{2B} \tag{8}$$

$$\delta_{cr} = \frac{\lambda_0 d}{L_{eff}} \tag{9}$$

Using these expressions, the range and cross-range resolutions were calculated to be 1.67 cm and 1.36 cm, respectively. In Eq. (8) c is the speed of light while B denotes the imaging bandwidth. In Eq. (9) λ_0 is the free-space wavelength, d is the imaging distance and L_{eff} is the effective aperture size of the overall system. For imaging, the reconstruction volume is discretized into 3D voxels. Dimensions of the discretization voxels are 1.5 cm in range (x-axis) and 1 cm in cross-range (yz-plane), selected in accordance with the calculated resolution limits of the system.

#258155 Received 26 Jan 2016; revised 26 Mar 2016; accepted 26 Mar 2016; published 14 Apr 2016

Given the cross-range resolution limit, δ_{cr} = 1.36 cm, we performed imaging of a resolution target to demonstrate the capability of the Mills-Cross imager to perform imaging at the diffraction limit. The reconstruction volume enclosing the imaged resolution target is 7.5 cm x 30 cm x 30 cm (17° FOV), resulting in N = 4,500 voxels. In order to solve Eq. (1) for image reconstruction, the matched filter technique is used. The reconstructed image of the resolution target is shown in Fig. 14. The values in the colorbar denote the normalized magnitude of the reconstructed reflectivity values (linear scale).

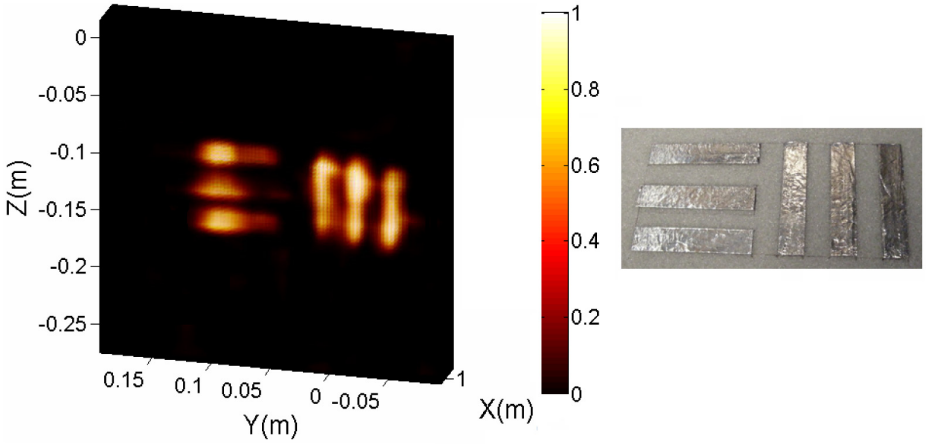

Fig. 14. Reconstructed image of a 1.5 cm resolution target together with a picture of the actual target.

Reconstructed image in Fig. 14 is plotted up-sampled by a factor of two in order to improve the smoothness of the image. As can be seen in Fig. 14, the outlines of the metal stripes are clearly visible, demonstrating the ability of the system to support imaging at the diffraction limit.

Following the resolution target, we performed imaging of an L-shaped phantom, representing a gun-shaped threat object. The reconstructed image of the L-shaped phantom is shown in Fig. 15, together with a photograph of the actual phantom. The reconstruction volume for this target is 7.5 cm x 20 cm x 20 cm, resulting in N = 2,000 voxels and providing a FOV of 11.4°. As can be seen in Fig. 15, the reconstructed image provides a reasonable reproduction of the L-shaped phantom. Artifacts due to specularity are anticipated since the object is highly reflective.

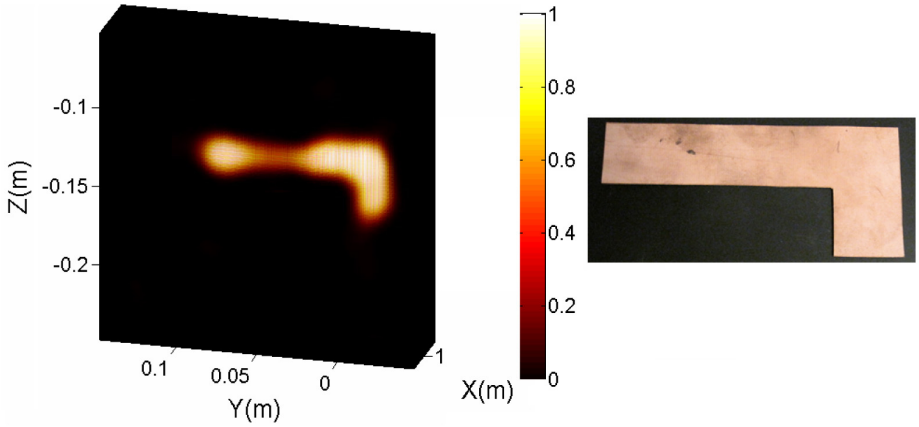

Fig. 15. Reconstructed image of an L-shaped phantom together with a picture of the actual target.

#258155 Received 26 Jan 2016; revised 26 Mar 2016; accepted 26 Mar 2016; published 14 Apr 2016

In Fig. 16, imaging of a word target, consisting of the individual letters forming the word "DUKE" was performed. In comparison to the objects imaged up to now, the information content of this target is higher. The imaging volume for this target is 7.5 cm (x-axis) x 40 cm (y-axis) x 30 cm (z-axis), resulting in N = 6,000 voxels with a FOV of 22.6° along the y-axis and 17° along the z-axis.

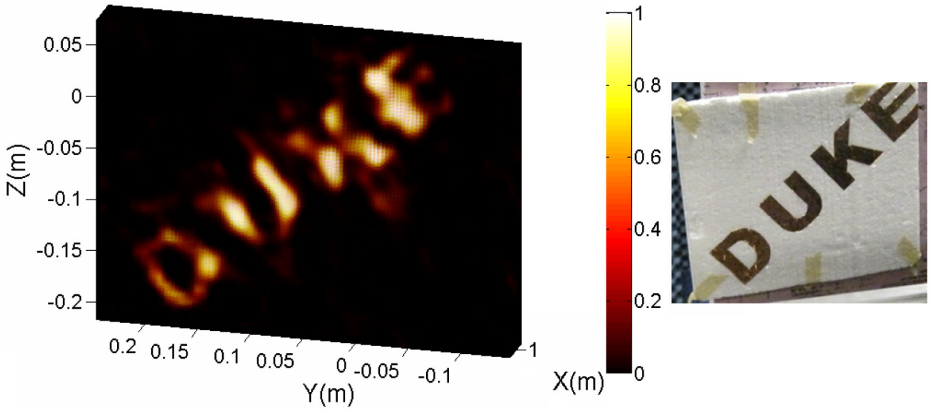

Fig. 16. Reconstructed image of word "DUKE" target together with a picture of the actual target.

As can be seen in Fig. 16, the reconstructed image clearly reveals the word "DUKE". The dynamic range for the reconstructed images demonstrated in Figs. 14-16 was 25 dB. The matched filter reconstruction algorithm is a non-iterative method, minimizing the amount of time required for image reconstruction. For the images reconstructed in this work, the reconstruction time was less than 0.04 seconds (Specifications of the computer used for image reconstruction are Intel® Core i7 CPU, 24 GB RAM and NVIDIA® Quadro® K5000 GPU).

7. Conclusion

We have demonstrated a frequency-diverse imaging system using printed cavity apertures consisting of circular irises distributed in a Mills-Cross pattern and operating over the K-band frequency regime. Adoption of the Mills-Cross structure optimizes the effective aperture pattern and maximizes the number of the Fourier components sampled in the k-space while minimizing the sampling redundancy. In comparison to the previously reported frequency-diverse apertures, the proposed Mills-Cross architecture improves the Q-factor and the information content of the modes collecting the imaging scene information. It has been proved through singular value spectrum analyses that the Mills-Cross configuration significantly reduces the correlation between the measurement modes. Imaging of a number of targets, including a 1.5 cm resolution target, has successfully been demonstrated, suggesting that the proposed imaging system supports imaging at the diffraction limit. The system can readily be scaled for imaging of more complex objects, such as human-sized targets, and extended to higher frequencies for applications where finer resolution limits are required.

Acknowledgment

This work was supported by the Department of Homeland Security, Science and Technology Directorate (Contract No. HSHQDC-12-C-00049). The published material represents the position of the author(s) and not necessarily that of the DHS. The authors would also like to acknowledge Rogers Corporation for their contribution of RF materials to the research effort.

#258155 Received 26 Jan 2016; revised 26 Mar 2016; accepted 26 Mar 2016; published 14 Apr 2016